International Journal of Heat and Mass Transfer 261 (2026) 128570

Contents lists available at ScienceDirect

International Journal of Heat and Mass Transfer

journal homepage: www.elsevier.com/locate/hmt

A multi-physics single-phase SPH scheme to simulate droplet interaction with a solid surface including thermo-capillary effects

Chunze Cen [a,*], Aaron English [b], Georgios Fourtakas [a], Steven Lind [c], Benedict D. Rogers [a]

[a] School of Engineering, Faculty of Science and Engineering, University of Manchester, Manchester M13 9PL, United Kingdom
[b] Department of Engineering and Architecture, University of Parma, Parma, Italy
[c] School of Engineering, Cardiff University, CF24 3AA, United Kingdom

ARTICLE INFO

Keywords:
Smoothed particle hydrodynamics
Temperature-dependent single-phase surface tension
Thermo-capillary flows
Marangoni forces
DualSPHysics

ABSTRACT

This paper presents a single-phase 3-D smoothed particle hydrodynamics (SPH) scheme to simulate thermo-capillary flows in micro-scale and nano-scale fluid engineering. This study focuses on droplet interaction with a solid surface that includes thermo-capillary forces known as Marangoni forces with temperature-dependent surface tension, heat transfer and buoyancy. To avoid excessive and prohibitive computational runtimes, the new formulation is implemented within the single-phase weakly compressible SPH formalism. While SPH is ideally suited to such highly nonlinear flows, little is known about the suitability of using SPH for the modelling of droplet-surface interactions with a single-phase model at the micro scale. The present work investigates the advantages and limitations of the new approach with the scheme being validated using 2-D and 3-D test cases including natural convection in a cavity, droplet impact on a solid surface, and droplet migration. Numerical results are in good agreement with the reference and experimental results. The extension to 3-D provides a more accurate prediction of the droplet displacement compared to previous SPH studies on droplet migration. The efficiency benefits in computing only one phase are significant, especially in 3-D. However, the final case of rapid droplet spreading on a surface highlights that the current single-phase model, whilst showing good agreement in the early stage of the flow, exhibits limitations in cases where the presence of a second phase needs to be considered.

1. Introduction

The droplet migration, when placed on a heated surface with a temperature gradient arising from the Marangoni effect, has attracted considerable research focus due to its potential applications in various droplet-based fluidic devices [1]. Physically, the Marangoni effect in such thermo-capillary flows is driven by surface shear stresses caused by the surface tension gradient, which results from the temperature gradient along the droplet interface. Indeed, the phenomenon of droplet migration has been widely studied numerically. Tseng et al. [2] conducted both experimental and three-dimensional (3-D) numerical studies, showing good agreement between the two. Using the level-set (LS) method [3], Sui [4] demonstrated that a droplet will migrate either towards the hot or the cold side, depending on its contact angle and the viscosity ratio between the droplet and the surrounding gas. Subsequently, Fath and Bothe [5] adopted the volume-of-fluid (VOF) approach [6] to extend droplet migration to 3-D, reporting numerical results consistent with those of Sui [4]. Leet al. [7] employed the finite element method (FEM) to investigate the transient migration of a micro-droplet within a micro-channel, revealing that the droplet first accelerates and then decelerates to rest under a temperature gradient. Fu et al. [8] used the lattice Boltzmann method (LBM) to study droplet migration on a series of wettability-confined tracks, demonstrating that surface confinement can accelerate migration, while the migration speed is influenced by geometry and wettability. In addition to these mesh-based methods, mesh-less and particle methods such as smoothed particle hydrodynamics (SPH) provide a promising alternative. Due to the diverse length and time scales arising from the small length and high mobility of the droplet, the SPH method is particularly appropriate due to its Lagrangian mesh-free formulation and its suitability for free-surface flows, compared to traditional mesh-based CFD methods.

Thermo-capillary flow involves multiple physical phenomena, among which surface tension is one of the most dominant. Surface tension arises from the unbalanced forces of the molecules at the fluid interface. The continuum surface force (CSF) model proposed by Brackbill et al. [9], in which surface tension is represented as a volumetric force, has been widely adopted in SPH. Many CSF-based surface tension

---

* Corresponding author.
E-mail address: chunze.cen@manchester.ac.uk (C. Cen).

https://doi.org/10.1016/j.ijheatmasstransfer.2026.128570
Received 2 December 2025; Received in revised form 25 January 2026; Accepted 17 February 2026

models and enhancements have been developed [10–16]. In thermo-capillary flows, as the surface tension varies with temperature, an additional force known as the Marangoni force arises due to the temperature gradients along the free-surface. This Marangoni effect must be incorporated into the surface tension model to accurately capture the flow. Tong & Browne [17] developed an incompressible multi-phase SPH model to study the thermo-capillary flow by investigating a single droplet immersed in a second phase. Hopp-Hirschler et al. [18] proposed a multi-phase SPH model to extend the research to more complex flows and provided step-by-step validation test cases as benchmarks for thermo-capillary flow in SPH. Meier et al. [19] proposed a model for thermo-capillary phase change in additive manufacturing and compared different temperature gradient approximations.

The aforementioned numerical approaches for simulating thermo-capillary flow are multi-phase models. While these models can provide a comprehensive view by capturing the interactions between liquid and gas phases, they are computationally expensive. The high computational cost arises due to the large number of SPH particles required to accurately represent both phases and resolve the dynamics at the liquid–gas interface. In addition, accurately simulating two phases with high density and viscosity ratios is a well-known challenge in SPH. This can lead to numerical issues, such as tensile instabilities at the interface. To address these problems, a very small time step is usually required, which further increases the computational cost. Given these challenges, a single-phase approach is desirable and motivates this study. Firstly, it vastly reduces the total number of particles, resulting in more efficient computations. Secondly, it simplifies the physical model and helps to avoid the numerical difficulties at the interface. This allows for a simplified model targeting the dominant physical phenomena within the fluid, providing a clear insight into the thermo-capillary effects. Among thermo-capillary flows, droplet migration has been understudied using SPH. Recently, Long et al. [20] developed an improved SPH method to study droplet migration under varying contact angles and viscosities, showing good agreement with experimental data. However, their result showed a deviation between the numerical and experimental results and lacked 3-D simulations. To address these limitations, this work provides a more accurate estimation of the displacement and 3-D results for droplet migration.

This paper aims to develop a single-phase SPH model to simulate the Marangoni effect, targeting the case of droplet migration on a heated surface with a temperature gradient. The Marangoni force model proposed by Bierwisch et al. [21] is employed to represent the effects of the gradient of surface tension. Heat conduction is modelled using the formulation proposed by Cleary & Monaghan [22]. The Oberbeck–Boussinesq (OB) approximation is introduced to simulate the buoyancy force. An acoustic damper term [23] is also applied to reduce acoustic pressure waves, especially in violent cases such as droplet impact on a solid surface. All these models are implemented in DualSPHysics 5.4. The DualSPHysics solver is an accurate and robust open-source solver based on the SPH method, specifically developed to simulate complex free-surface flows and fluid–structure interactions on both CPU and GPU architectures [24]. The solver has been extensively validated through several benchmark cases, including coastal engineering, fluid–solid interaction, and astrophysics. Given that a single-phase surface tension model [25] has been implemented in DualSPHysics [26], this work investigates droplet migration using the aforementioned variant of DualSPHysics.

This paper is organized as follows: Section 2 presents the governing equations and the methods including boundary conditions, time integration, surface tension formulations, and the Marangoni effect. In Section 3, the model is validated against three benchmark test cases, including natural convection, droplet impact on a solid surface, and droplet migration. The limitations of the model are then demonstrated via the case of droplet rapid spreading with Marangoni effect. This paper ends in Section 4 with conclusions and future work.

2. Numerical methods

2.1. Governing equations

In this paper, we consider the Navier–Stokes equations in Lagrangian form and the weakly-compressible SPH (WCSPH) is applied. In WCSPH, the Lagrangian form of the conservation of mass, momentum and energy equations are written as follows,

$$\begin{aligned}\frac{D\rho}{Dt} &= -\rho\nabla\cdot\mathbf{u},\\ \frac{D\mathbf{u}}{Dt} &= -\frac{1}{\rho}\nabla p + \frac{1}{\rho}\nabla\cdot\boldsymbol{\tau} + \mathbf{F}_{body},\\ \frac{DT}{Dt} &= \frac{k_T}{C_p\rho}\nabla^2 T,\end{aligned} \tag{1}$$

where ρ is density, $\mathbf{u}$ denotes velocity, p represents pressure, $\boldsymbol{\tau}$ signifies the shear stress tensor, $\mathbf{F}_{body}$ corresponds to the body force, T refers to temperature, k_T stands for thermal conductivity, and C_p represents heat capacity at constant pressure. In this paper, the body force may contain gravity, surface tension force and Oberbeck–Boussinesq approximation term.

2.2. SPH discretization

Based on the DualSPHysics formulation [24], and applying the laminar viscosity from [27], the following discrete formulations of the governing equations can be obtained,

$$\begin{aligned}\frac{D\rho_i}{Dt} &= \rho_i\sum_j\frac{m_j}{\rho_j}\mathbf{u}_{ij}\cdot\nabla_i W_{ij},\\ \frac{D\mathbf{u}_i}{Dt} &= -\sum_j m_j\left(\frac{p_i+p_j}{\rho_i\rho_j}\right)\nabla_i W_{ij} + \sum_j m_j\frac{2(\nu_i+\nu_j)}{\rho_i+\rho_j}\left(\frac{\mathbf{r}_{ij}\cdot\nabla_i W_{ij}}{\mathbf{r}_{ij}^2+0.001h^2}\right)\mathbf{u}_{ij} + \mathbf{F}_{body},\\ \frac{DT_i}{Dt} &= -\frac{1}{C_{p,i}}\sum_j\frac{m_j}{\rho_i\rho_j}(k_{T,i}+k_{T,j})(T_i-T_j)\frac{\mathbf{r}_{ij}\cdot\nabla_i W_{ij}}{\mathbf{r}_{ij}^2+0.001h^2}.\end{aligned} \tag{2}$$

where the subscripts i and j refer to the ith interpolating and jth neighbouring particle, m denotes the particle mass, W_{ij} is the kernel evaluated between particle i and j, ν is the kinematic viscosity and $\mathbf{r}_{ij} = |\mathbf{r}_i - \mathbf{r}_j|$ denotes the distance between particle i and j. The term $0.001h^2$ is introduced to prevent the singularity when r_{ij} tends to zero, where h represents the smoothing length. The current energy equation formulation does not guarantee that the heat flux is continuous across material interfaces [22]. Thus, Cleary et al. [22] proposed a corrected energy formulation.

The SPH version of conservation of energy is therefore expressed as:

$$\frac{DT_i}{Dt} = -\frac{1}{C_{p,i}}\sum_j\frac{m_j}{\rho_i\rho_j}\frac{4k_{T,i}k_{T,j}}{k_{T,i}+k_{T,j}}(T_i-T_j)\frac{\mathbf{r}_{ij}\cdot\nabla_i W_{ij}}{\mathbf{r}_{ij}^2+0.001h^2}. \tag{3}$$

Within weakly compressible SPH, an equation of state is used to close the system of governing equations. The equation of state uses an artificial speed of sound to ensure that the density fluctuation is less than 1%. In this paper, Tait's equation is used [24],

$$p = \frac{c_o^2\rho_o}{\gamma}\left[\left(\frac{\rho}{\rho_o}\right)^\gamma - 1\right], \tag{4}$$

where c_o is the reference speed of sound, γ is a constant known as the polytropic index of the fluid (typically 7 for the water and 1,4 for the air), and the subscript o denotes the reference value.

2.3. Surface tension force

The surface tension force can be decomposed into normal and tangential forces to the surface,

$$\mathbf{F}_s = \mathbf{F}_{s,n} + \mathbf{F}_{s,t}. \tag{5}$$

where the subscript s denotes the surface tension, and, n and t denote the normal and tangential components, respectively. The surface tension force can be transferred from a surface force to a volume force based on the continuum surface force (CSF) model [9],

$$\mathbf{F}_s = (-\sigma\kappa\mathbf{n}_i + \nabla_t\sigma)\delta_s \tag{6}$$

where σ is the surface tension coefficient, κ denotes the curvature of the interface, δ_s is the interfacial function and $\mathbf{n}$ is the unit normal vector to the interface. The unit vector normal to the interface from Vergnaud et al. [25] is expressed as,

$$\mathbf{n}_i = -\frac{\nabla\lambda_i}{\|\nabla\lambda_i\|}, \tag{7}$$

where

$$\nabla\lambda_i = \sum_j(\lambda_j - \lambda_i)(\mathbb{L}_i\nabla W_{ij})V_j, \tag{8}$$

and λ_i is the minimum eigenvalue of the matrix $\mathbb{L}_i^{-1}$. The $\mathbb{L}_i^{-1}$ matrix is the inverse of correction matrix $\mathbb{L}_i$ [25] defined as,

$$\mathbb{L}_i^{-1} = \sum_j(\mathbf{r}_j - \mathbf{r}_i)\otimes\nabla_i W_{ij}V_j. \tag{9}$$

The surface curvature of particle i can be evaluated as,

$$\kappa_i = \sum_j \mathbb{L}_i(\mathbf{n}_j - \mathbf{n}_i)\cdot\nabla_i W_{ij}V_j. \tag{10}$$

In the single-phase model, the interfacial function is expressed as,

$$\delta_{s,i} = 2\|\nabla_i W_{ij}V_j\|. \tag{11}$$

To improve the accuracy and robustness of the model for thin jet tips or small droplets, several corrections have been implemented, following the approach of [25].

For the cases including solid boundaries, the evaluation of the normal vector near the solid boundary should be corrected for better accuracy. The definition sketch of the normal correction procedure near the contact line, which is adapted from [25], is shown in Fig. 1.

Based on [25], the tangent vector $\mathbf{t}_{b,i}$ to the boundary which is also normal to the contact line is expressed as,

$$\mathbf{t}_{b,i} = \frac{\mathbf{n}_i - (\mathbf{n}_i\cdot\mathbf{n}_{b,i})\mathbf{n}_{b,i}}{\|\mathbf{n}_i - (\mathbf{n}_i\cdot\mathbf{n}_{b,i})\mathbf{n}_{b,i}\|}, \tag{12}$$

where $\mathbf{n}_{b,i}$ is the approximate unit wall normal pointing away from the wall towards the fluid and computed for near-wall fluid particle i via summation over the kernel gradient of nearby wall particles j [28],

$$\mathbf{n}_{b,i} = \frac{\sum_j\nabla_i W_{ij}}{|\sum_j\nabla_i W_{ij}|}. \tag{13}$$

Then, the corrected normal $\mathbf{n}^*$ for particle i is defined as,

$$\mathbf{n}_i^* = \cos\theta_i^*\mathbf{n}_{b,i} + \sin\theta_i^*\mathbf{t}_{b,i}, \tag{14}$$

where θ_i^* is the corrected contact angle and expressed as,

$$\theta_i^* = \begin{cases} \theta_e + (\theta_i - \theta_e)(d_i/R)^2 & \text{if } d_i < R, \\ \theta_i \quad \text{otherwise}, & \end{cases} \tag{15}$$

where $R = 2h$ is the kernel radius, d_i is the distance from fluid particle i to the nearest boundary which is calculated through $d_i = \min_{j\in wall}\mathbf{r}_{ij}\cdot\mathbf{n}_i$, θ_e denotes the equilibrium contact angle and θ_i is the contact angle before correction defined as,

$$\theta_i = \arccos(\mathbf{n}_i\cdot\mathbf{n}_{b,i}). \tag{16}$$

During the simulation, the computed normal $\mathbf{n}_i$ is replaced by the corrected $\mathbf{n}_i^*$ before the computation of curvature.

The normal component of the surface tension force in a single-phase system has been detailed in [25,26]. The tangential component $\nabla_t\sigma$, which is also known as the Marangoni force, is due to the temperature-dependent gradient of surface tension. Following Tong & Brown [17], it is defined as,

$$\nabla_t\sigma = \frac{\partial\sigma}{\partial T}\nabla_t T, \tag{17}$$

where $\partial\sigma/\partial T$ is the temperature coefficient of the surface tension, typically negative, driving the Marangoni flow from warm regions towards cold regions along the surface [21].

The tangential component of the gradient of temperature $\nabla_t T$ is given as,

$$\nabla_t T_i = \nabla T_i - (\nabla T_i\cdot\mathbf{n}_i)\mathbf{n}_i. \tag{18}$$

The gradient of temperature is obtained by,

$$\nabla T_i = \sum_j\frac{m_j}{\rho_j}(T_j - T_i)\mathbb{L}_i\nabla_i W_{ij}. \tag{19}$$

2.4. Oberbeck–Boussinesq approximation

The Oberbeck–Boussinesq (OB) approximation is the most common approach in incompressible or weakly-compressible methods to model the buoyancy-driven flows. It assumes that the change in density due to temperature difference is neglected except in the buoyancy term of momentum equation. Thus, the flow is approximately incompressible and the OB term $\mathbf{F}_B$ is defined as:

$$\mathbf{F}_B = \rho(-\beta_{exp}(T - T_0))\mathbf{g}, \tag{20}$$

where β_{exp} is the thermal expansion coefficient.

2.5. Particle shifting

The particle shifting algorithm is a useful method to improve the particle distribution and increase the accuracy and numerical stability.

Lind et al. [29] proposed a particle shifting algorithm based on the Fick's law of diffusion, which gives,

$$\mathbf{J} = -\mathscr{D}'\nabla C, \tag{21}$$

where $\mathbf{J}$ denotes the diffusion flux, $\mathscr{D}'$ presents the diffusion coefficient and C is the concentration. The concentration gradient ∇C is expressed in SPH method as,

$$\begin{aligned} C_i &= \sum V_j W_{ij}, \\ \nabla C_i &= \sum_j V_j\nabla_i W_{ij}. \end{aligned} \tag{22}$$

Thus, the particle shifting distance $\delta\mathbf{r}$ is,

$$\delta\mathbf{r}_i = -\mathscr{D}\nabla C_i, \tag{23}$$

where $\mathscr{D}$ is a new diffusion coefficient, which is proportional to $\mathscr{D}'$.

The coefficient $\mathscr{D}$ is determined by the von-Neumann stability criterion as,

$$dt \le 0.5\frac{h^2}{\mathscr{D}}. \tag{24}$$

Thus, based on Lind et al. [29], the particle shifting distance $\delta\mathbf{r}_i$ is,

$$\delta\mathbf{r}_i = -A_s h^2\nabla C_i, \tag{25}$$

where A_s is a case-dependent coefficient. The maximum allowable shifting distance should be less than $0.2h$ to avoid the particle penetration into the wall particles.

Additionally, based on the normal an tangential components of the gradient of concentration as follows,

$$\nabla C_i = \frac{\partial C_i}{\partial n_i}\mathbf{n}_i + \frac{\partial C_i}{\partial s_i}\mathbf{s}_i; \quad \frac{\partial C_i}{\partial n_i}\mathbf{n}_i = (\mathbf{n}_i\cdot\nabla C_i)\mathbf{n}_i. \tag{26}$$

Lind et al. [29] provides the following equation for the particles near or at the free-surface with a large concentration gradient,

$$\delta\mathbf{r}_i = -\mathscr{D}\left(\frac{\partial C_i}{\partial s_i}\mathbf{s}_i + \alpha_p\left(\frac{\partial C_i}{\partial n_i} - \beta_p\right)\mathbf{n}_i\right), \tag{27}$$

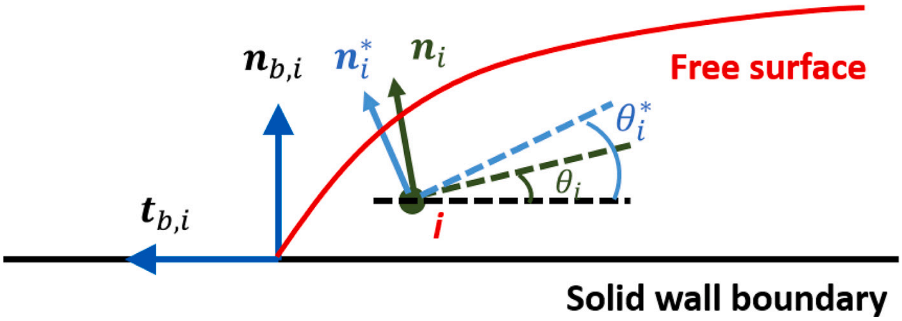

Fig. 1. Definition sketch of the normal correction procedure near the contact line.
Source: Adapted from [25].

where $\mathbf{s}_i$ and $\mathbf{n}_i$ denote the tangent and normal unit vectors to the free-surface. The constants α_p and β_p are two tuning parameters.

However, depending on the values of these parameters, an unphysical gap between the free-surface and the fluid bulk particles and the unphysical diffusion of the free-surface particles can be observed. To solve these problems, Khayyer et al. [30] proposed the so-called optimized particle shifting (OPS) methods without the tuning parameters α_p and β_p. The OPS begins by determining the corrected unit normal vector,

$$\mathbf{n}_i = -\frac{\mathbb{L}_i \cdot \nabla C_i}{|\mathbb{L}_i \cdot \nabla C_i|}; \tag{28}$$

Considering that the normal term to the interface should be theoretically zero [30], the particle shifting distance $\delta\mathbf{r}_i$ should be,

$$\delta\mathbf{r}_i = -Ah^2(\nabla C_i - (\mathbf{n}_i \cdot \nabla C_i)\mathbf{n}_i) = -Ah^2(\mathbf{I} - \mathbf{n}_i \otimes \mathbf{n}_i) \cdot \nabla C_i. \tag{29}$$

The OPS method is used for all cases in this study.

2.6. Acoustic damper term

During the violent droplet-surface impact, a strong acoustic wave is generated which results in noise in the pressure field. Recently, Sun et al. [23] proposed a new diffusion term, which is called the acoustic damper term, to dissipate the unphysical acoustic wave. The viscous term in the momentum equation can be expressed as,

$$\frac{1}{\rho}\nabla \cdot \tau = \nabla \cdot \left(\mu(\nabla\mathbf{u} + \nabla\mathbf{u}^{\top}) - \lambda_{vis}(\nabla \cdot \mathbf{u})\mathbf{I}\right), \tag{30}$$

where λ_{vis} is the second coefficient of viscosity and $\mathbf{I}$ denotes the identity matrix.

Looking the second viscosity term in the momentum equation, it can be written in SPH form [23],

$$\begin{aligned} \lambda_{vis}\nabla(\nabla \cdot \mathbf{u}) &= \lambda_{vis}\sum_j \left[(\nabla \cdot \mathbf{u})_j + (\nabla \cdot \mathbf{u})_i\right]\nabla_i W_{ij} V_j, \\ (\nabla \cdot \mathbf{u})_i &= \sum_j \mathbf{u}_{ij} \cdot \nabla_i W_{ij} V_j. \end{aligned} \tag{31}$$

Therefore, the acoustic damper term in momentum equation is written as,

$$\left(\frac{D\mathbf{u}_i}{Dt}\right)_{acoustic} = \frac{1}{\rho}\mathbf{F}_{acoustic} = \frac{1}{\rho}\lambda_{vis}\nabla(\nabla \cdot \mathbf{u}). \tag{32}$$

2.7. Boundary condition

The modified dynamic boundary condition (mDBC) of DualSPHysics is used in this study due to its accurate estimation of density on boundary particles and the reduction of an unphysical gap between the fluid and boundary particles present in the original dynamic boundary conditions (DBC) [31]. In the mDBC method, a ghost particle g for each boundary particle b is projected into the fluid domain and fluid properties are sampled using a Liu and Liu corrected kernel sum [32]. In 2D, density, ρ_g is found at the ghost particle by solving the following linear system

$$\mathbf{A}_g\left[\rho_g, \partial_x\rho_g, \partial_z\rho_g\right]^T = \left[\sum_j m_j W_{gj}, \sum_j m_j \partial_x W_{gj}, \sum_j m_j \partial_z W_{gj}\right]^T \tag{33}$$

where $\mathbf{A}_g$ is the Liu and Liu correction matrix. More details on the construction of the linear system can be found in [31]. In the latest iteration of mDBC [33], the density of the boundary particle, ρ_b, is found through a pressure cloning procedure

$$P_g = c_0^2\left(\rho_g - \rho_0\right) \tag{34}$$

$$P_b = P_g + \rho_0\left[(\mathbf{g} - \mathbf{a}_b) \cdot \mathbf{n}_b\right]\left[(\mathbf{r}_g - \mathbf{r}_b) \cdot \mathbf{n}_b\right] \tag{35}$$

$$\rho_b = \rho_0 + P_b/c_0^2 \tag{36}$$

where P_g and P_b are the ghost and boundary particle pressures respectively, c_0 is the speed of sound and ρ_0 is the reference density of the fluid. The vectors $\mathbf{g}$ and $\mathbf{a}_b$ are the acceleration due to gravity and the acceleration of the boundary particle respectively, and $\mathbf{n}_b$ is the normal vector that points from a boundary particle to its ghost node (note, the boundary normal is not of unit length).

To apply a no-slip boundary condition, the velocity of a boundary particle is given as [34],

$$\mathbf{u}_b = 2\mathbf{u}_w - \mathbf{u}_g, \tag{37}$$

where the $\mathbf{u}_w$ is the velocity of the wall and $\mathbf{u}_g$ is the velocity of the ghost boundary obtained through a Shepard sum,

$$\mathbf{u}_g = \frac{\sum_j \mathbf{u}_j W_{gj} V_j}{\sum_j W_{gj} V_j}. \tag{38}$$

Finally, an additional no-penetration condition is applied for the small number of fluid particles that are likely to penetrate and leak through the boundaries. As detailed in [33] and available in v5.4 of DualSPHysics [24], fluid particles that are deemed close to boundary particles, between $0.75dp$ and $0.25dp$, and that are moving towards the boundary relative to the boundary motion are redirected to prevent penetration. This redirection is applied through a distance weighted correction to the fluid particle's velocity with a larger correction applied for smaller distances.

To handle the heat exchange with the solid boundary, the adiabatic boundary condition as detailed in Reece et al. [35] is applied. For an adiabatic boundary, following the mDBC method, the temperature of the boundary particle is obtained by projecting a ghost particle g into the fluid domain and then updating the boundary particle using the mirrored value from its corresponding ghost node $T_i = T_{ig}$. In this way, there is no temperature gradient across the boundary, effectively blocking heat transfer through the boundary.

2.8. Time integration

The symplectic predictor–corrector method implemented in DualSPHysics [24,36] is employed in this work. The first step in this time stepping method is to predict the dependent variables at half time-step $t + dt/2$. Then, these variables are corrected using the predicted time derivatives at half time-step $t+dt/2$. Finally, the corrected variables are used to update the new value at next time-step $t + dt$.

2.8.1. Time-step criteria

In numerical analysis, a sufficiently small time-step is required for an explicit time integration method. Based on the Courant–Friedrichs–Lewy (CFL) condition, the variable time step is obtained by the following criteria. The first criterion depends on the acceleration,

$$\Delta t_f = C_f \min_i\left(\sqrt{h/|\mathbf{a}|_{\max_i}}\right), \tag{39}$$

where $C_f = 0.1$ denotes the Courant number for this criterion, $\mathbf{a}$ is the total acceleration (or force per unit mass) of the particle and $|\mathbf{a}|_{max_i}$ is the maximum acceleration among all particles.

The time step constraint for the CFL condition is given by,

$$\Delta t_{avis} = C_{avis} \min_i \frac{h}{c_o + \max_j \frac{|h\mathbf{u}_i \cdot \mathbf{r}_{ij}|}{|\mathbf{r}_{ij}|^2 + 0.01h^2}}, \tag{40}$$

where $C_{avis} = 0.1$ for this criterion.

Both of the above time step constraints have traditionally used in the DualSPHysics solver. Due to the presence of the surface tension, an additional stability criterion is required to be added which is given by [25],

$$\Delta t_{st} = C_{st} \min_i\left(\sqrt{\frac{\rho_i R_k^2}{2\pi\sigma|\kappa_i|}}\right), \tag{41}$$

where $C_{st} = 0.05$ is used for this criterion [25] and R_k is the smoothing kernel radius (typically $R_k = 2h$).

It should be noted that due to the explicit space and time integration of the adopted weakly compressible SPH, the Courant numbers are conservative to ensure stability. This is especially true for the CFL and force criterion where acoustic waves due to impact propagate in the domain. Herein, the recommended values from the DualSPHysics solver have been adopted together with the C_{sf} for the surface tension adopted by [25,26].

Then the appropriate variable time-step is defined as:

$$\Delta t = \min(\Delta t_f, \Delta t_{vis}, \Delta t_{st}). \tag{42}$$

3. Results and discussion

This section presents the numerical results and benchmark validation for the proposed SPH model. First, the model is validated through natural convection and droplet impact cases. Subsequently, droplet migration on a heated surface is investigated. Followed by an analysis of rapid droplet spreading. All simulations were performed on an NVIDIA RTX 5000 GPU to ensure computational efficiency.

3.1. Natural convection

The buoyancy-driven flow is validated using natural convection in a heated cavity. Two key non-dimensional parameters are considered here. The first one is the Prandtl number which expresses the ratio of viscous diffusion to the thermal diffusion, defined as:

$$Pr = \frac{\mu C_p}{k_T}. \tag{43}$$

where μ is the dynamic viscosity.

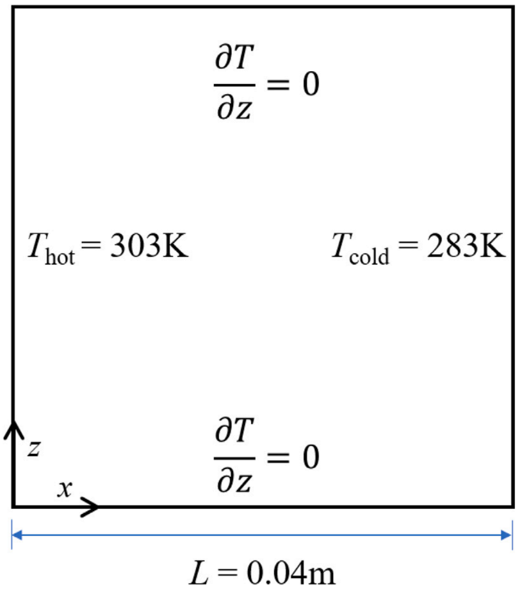

Fig. 2. Definition sketch for natural convection in a square cavity.

The second is the Rayleigh number which introduces the ratio of buoyancy to thermal diffusion, defined as:

$$Ra = \frac{g\beta_{exp} L_o^3 (T_{hot} - T_{cold}) C_p}{\nu k_T}. \tag{44}$$

where β_{exp} is the thermal expansion coefficient, and L_o is the characteristic length which corresponds to the length of the cavity in this case.

Based on the relevant setup of natural convection case by Reece [35], air within a cavity with initial room temperature $T_{air} = 293$ K, $Pr = 0.71$ and $Ra = 10^5$ is compared with the result in Wan et al. [37]. The geometry is shown in Fig. 2. The left wall at $x = 0$ m ($T_{hot} = 303$ K) and right wall at $x = 0.04$ m ($T_{cold} = 283$ K) hold a constant temperature during the simulation so that the temperature difference is fixed at 20 K. The top and bottom walls are adiabatic so that the physical boundary condition to be imposed is $\partial T/\partial z = 0$. The common method to impose adiabatic walls in SPH is to set the conductivity coefficient $k_T = 0$ on boundary particles so that they do not contribute to the heat transfer [35]. However, this method results in insufficient particles inside the kernel support of the fluid particles near the boundary when computing a change in temperature, and subsequently the kernel truncation error is introduced when computing the temperature. To improve the boundary treatment and reduce kernel truncation error, the mDBC method is used here. Similar to the density, the temperature of boundary particles is also obtained by the ghost particles within the fluid without the extrapolation, i.e. $T_i = T_g$ [35]. The no-slip boundary condition is applied to the velocity.

The length of the cavity is $L = 0.04$ m and to investigate convergence, three particle spacing are chosen as $dp = 0.001$ m, 0.0005 m and 0.00025 m which gives 1600, 6400 and 25,600 fluid particles, respectively, corresponding to the resolution in Wan et al. [37]. The smoothing length is set as $h = 2dp$. The flow parameters are shown in Table 1. It is worth noting that gravity is set to -8.821 m/s^2 to make $Ra = 10^5$. Gravity appears only in the OB term. A high speed of sound is chosen $c_0 = 80|\mathbf{u}_{max}| = 5$ m/s to increase the incompressibility since the flow is assumed to be incompressible with the OB effect. The simulation became unstable when using a low speed of sound such as $c_0 = 10|\mathbf{u}_{max}| = 0.625$ m/s as we observed a highly disordered particle distribution. The fluid particles have an initial uniform temperature distribution of $T_{air} = 293$ K which is also the reference temperature in the OB term.

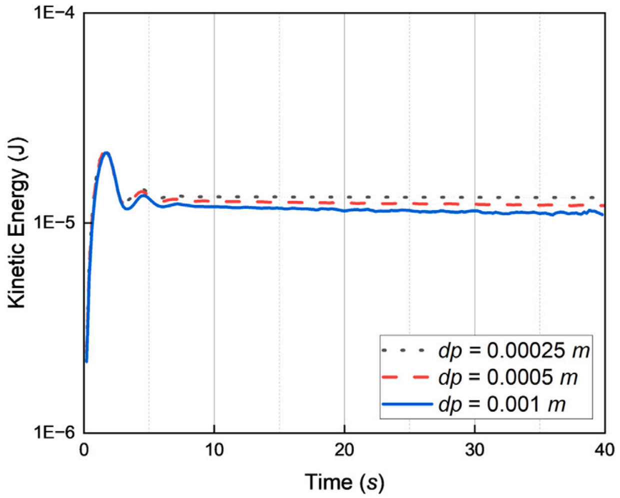

Fig. 3. Variation of total kinetic energy with time for the three different particles resolutions for the natural convection case.

Table 1
Parameters and values for the natural convection case.

Parameters	Value
ρ	$1.204\ \mathrm{kgm^{-3}}$
ν	$1.506 \times 10^{-5}\ \mathrm{m^2s^{-1}}$
C_p	$1.006 \times 10^3\ \mathrm{Jkg^{-1}K^{-1}}$
k_T	$0.02587\ \mathrm{Wm^{-1}K{-}1}$
β_{exp}	$3.43 \times 10^{-3}\ \mathrm{K^{-1}}$
g	$-8.821\ \mathrm{ms^{-2}}$

The following parameters are non-dimensionalized as:

$$\begin{aligned} x^* &= \frac{x}{L}, \\ u^* &= \frac{uL\rho C_p}{k_T}, \\ T^* &= \frac{T - T_{cold}}{T_{hot} - T_{cold}}, \\ t^* &= \frac{tk_T}{L^2\rho C_p}. \end{aligned} \tag{45}$$

The results are compared to Wan et al. [37] where a high-order discrete singular convolution method is used to investigate buoyancy-driven problems. Wan et al. [37] found that the flow reached steady state at $t = 34.88$ s. The variation of total kinetic energy with time is shown in Fig. 3. Herein, the difference of the kinetic energy (E_Δ) between two successive iterations (E_k^{n+1}, E_k^n) is used as the criterion for the system to be considered at the steady state, which is defined as $E_\Delta = |E_k^{n+1} - E_k^n| < 10^{-7}$. For the above parameters the system reaches steady state after 10 s. To ensure that this behaviour is maintained, the simulation is extended to 40 s.

Fig. 4 shows the dimensionless temperature (on the left hand side) and vertical velocity (on the right hand side) along the horizontal mid-line $z = L/2$ for three different resolutions. The SPH results are obtained along the line $z = L/2$ by the interpolation measure tool in DualSPHysics. The data from Wan et al. [37] is also drawn in the figure to compare with the SPH result. It can be seen that the SPH results agree well with that of Wan et al. [37]. Near the boundary the agreement worsens, but we note that the measured point $x = 0, L$ is not exactly on the boundary due to the limitations of the measure tool in DualSPHysics. In this measure tool, the interpolated velocity is computed using velocity values of neighbouring particles. Indeed, it can be observed that the finer the resolution, the closer the SPH result tends to the reference result of Wan et al. [37] due to the measured point being closer to the boundary.

Table 2
Parameters of two droplet impact test cases adopted from Šikalo et al. [38].

Parameters	Test 1	Test 2
Fluid	Glycerin	Water
ρ	$1220\ \mathrm{kg/m^3}$	$996\ \mathrm{kg/m^3}$
μ	0.116 Pa s	0.001 Pa s
σ	0.063 N/m	0.073 N/m
θ_{eq}	95^o	100^o
U_{impact}	1.04 m/s	1.64 m/s
Surface	Wax	Wax
We	51	90
Re	27	4010

3.2. 3-D droplet impact

Two more rigorous validation test cases are conducted herein, involving the dynamic evolution of a single droplet impacting on a flat solid surface.

Šikalo et al. [38] presented an experimental investigation of a single droplet impact onto a dry surface and its numerical simulation. Following the 5th and 7th experiment in the Table II from Šikalo et al. [38], the test cases with low and moderate Reynolds number are presented. The parameters are shown in Table 2. It is noted that the diameter of the droplet in both cases is $D = 2.45$ mm.

At first, the case with a relatively low Reynolds number $Re = 27$, where a glycerin droplet impacts on a solid wax surface, is presented (Test 1 in Table 2). Three initial inter-particle distances are chosen as $dp = 0.1$ mm, 0.05 mm and 0.025 mm, giving 9563, 68,420 and 514,255 fluid particles, respectively. The corresponding computational times are 208 s, 723 s and 6876 s, respectively The smoothing length is $h = 2dp$. The particle shifting technique from Khayyer et al. [30] is used due to its accurate free-surface shifting.

The impact process and the pressure distribution from the side and top view are shown in Figs. 5 and 6, respectively. The pressure is scaled with respect to the Laplace pressure. The non-dimensional time is set to $t^* = tU_{impact}/D$. The spreading factor $\beta_s = d/D$, which is the ratio of the spreading diameter d to the initial diameter of the droplet D, is compared using the SPH result and the experimental data from Šikalo et al. [38] as shown in Fig. 7. It is found that the SPH result converges to the experimental data.

This test case demonstrates that the current model is able to accurately describe the droplet impact case with a relatively low Reynolds number. The droplet impact case with a moderate Reynolds number $Re = 4010$ is also tested here (Test 2 in Table 2). The initial inter-particle distances are the same with Test 1 and the corresponding computational times are 453 s, 1565 s and 13,435 s, respectively. To ensure the numerical stability and accuracy of the high-Re impact process, several standard SPH treatments are implemented. These treatments are important to keep a physically consistent representation of the flow under high-velocity impact conditions.

First, the acoustic damper term from Sun et al. [23] is used here to reduce the acoustic pressure. The pressure waves propagate to the free surface initiating instabilities. This damper helps suppress the ejection of particles at the edge of the lamella at the moment when the droplet touches the surface. Secondly, in addition to the laminar viscosity term, a small amount of artificial viscosity is also required to stabilize the fluid, where the typical coefficient $\alpha_{vis} = 0.02$ is adopted based on our experience. The additional viscous term is foreseeable, as the Riemann solver used in the Ref. [25] provides more numerical diffusion. In [25], a MUSCL reconstruction scheme is used to reconstruct the left and right states of a Riemann problem and obtain accurate and stable results. It is noted that it is common for the artificial viscous coefficient to be calibrated for a specific case, whilst the diffusion in the Riemann solver is diffusion by design. Similar to the effect of the acoustic damper term, the artificial viscosity helps to avoid the ejection

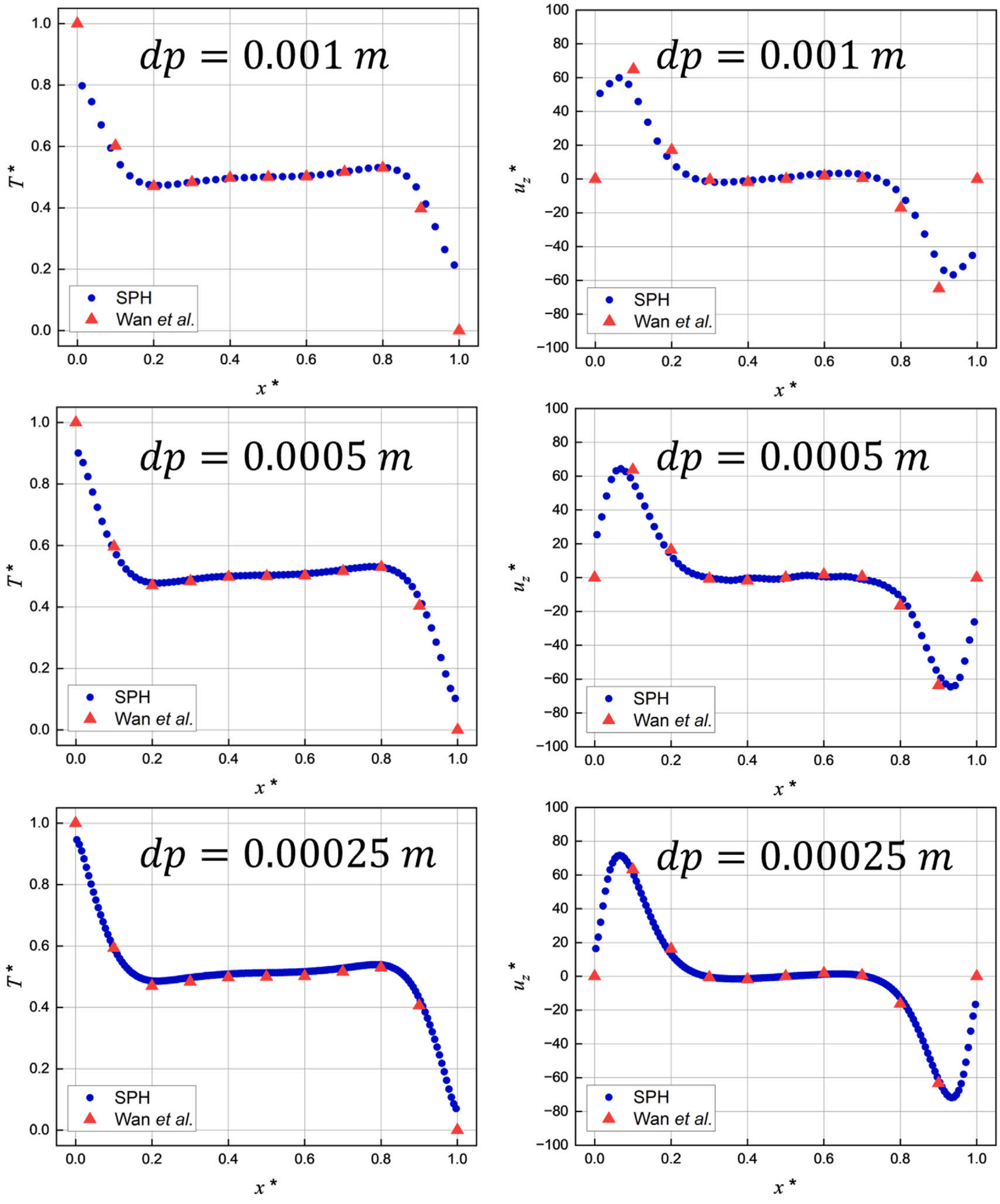

Fig. 4. Results of the natural convection cases for different particle resolutions. Left: Dimensionless temperature (T^*) along horizontal mid-line $z = L/2$; Right: Dimensionless vertical velocity (u_z) along horizontal mid-line $z = L/2$. The compared benchmark results are obtained from Wan et al. [37].

of particles. In addition, it can also help prevent the separation of the lamella from the droplet disk. Thirdly, the shifting criterion from Sun et al. [39] is adopted, where the particle shifting technique is switched off for free-surface particles with minimum eigenvalue less than 0.4. This is because the particle shifting technique can induce spurious numerical effects for such free-surface particles whose normal vectors might be inaccurately estimated due to the incomplete kernel support [39]. Switching off the particle shifting on free-surface particle helps to obtain a smooth discretization of the free surface and normal vector calculations which is essential in the surface tension forces calculation.Finally, a more restrictive criterion is applied such that the surface normal vector of an interior particle (defined by the minimum eigenvalue of the matrix $\lambda_i > 0.75$) is set to 0. This is a physically-motivated correction designed for the single-phase framework. This is because we find that the very thin gap between the lamella and the solid surface during the droplet impact and spreading process, which is physical [40], numerically led to an overestimation of the gradient of the minimum eigenvalue $\nabla\lambda_i$. As a consequence, the normal of a few interior particles located at the bottom of the lamella may not be exactly 0, resulting in the existence of the surface tension on these particles and introducing additional error.

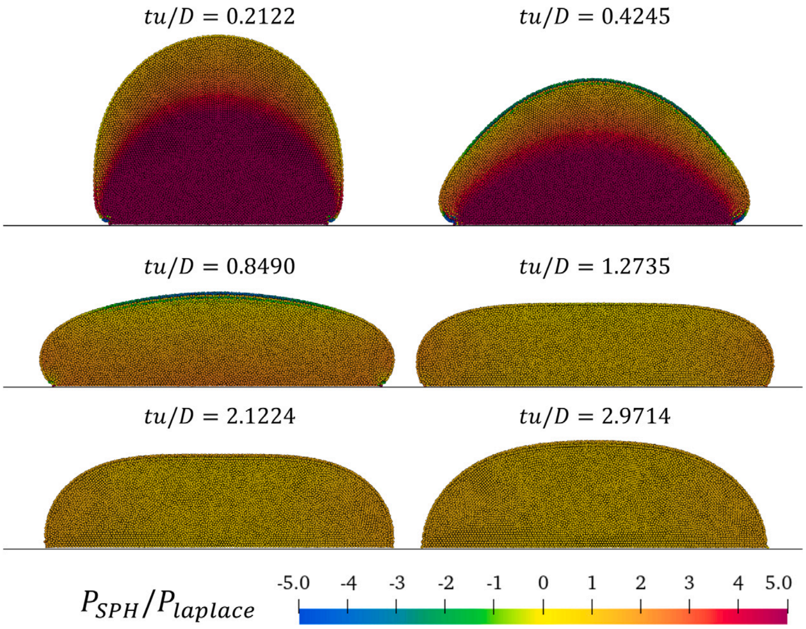

Fig. 5. The side view of a glycerin droplet impacting on a solid wax surface with the pressure distribution. The particle distance is $dp = 0.025$ mm. $Re = 27$.

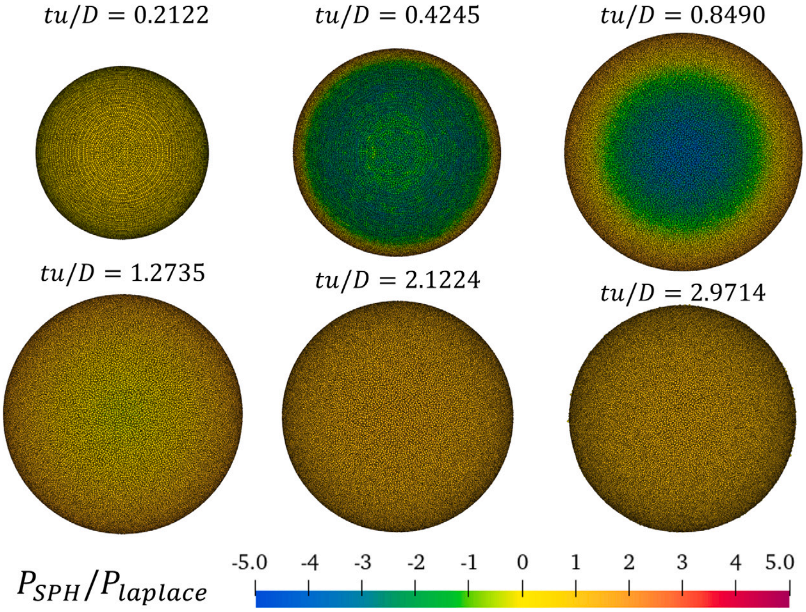

Fig. 6. The top view of a glycerin droplet impacting on a solid wax surface with the pressure distribution. The particle distance is $dp = 0.025$ mm. $Re = 27$.

In this case, we first tried the same initial inter-particle distances $dp = 0.1$ mm, 0.05 mm and 0.025 mm. However, unphysical break-up behaviour is observed even though the above methods are applied for the cases with $dp = 0.1$ mm and 0.05 mm. The process of the breakup is shown in Fig. 8. This breakup might be due to the very thin liquid film created during impact where the small number of particles over the depth of such a film is not able to accurately capture the behaviour. It is found that the minimal film thickness h_{min} satisfies the scaling law, which is observed both experimentally and numerically [41–44], as follows,

$$h_{min} \sim DRe^{-2/5}. \tag{46}$$

The breakup does not happen in the more resolved case with $dp = 0.025$ mm. The side view and the top view of the water droplet impact process with the pressure distribution are shown Fig. 9 and 10, respectively. The Rayleigh–Plateau instability can be observed on the film during the receding process from the side view. Additionally, the instability at the rim from the top view, which is also observed in the experiment, can be captured. The above two characteristics demonstrate the ability of the current model to describe such complex physics. However, it should be noted that several particles are left on the surface see the sub-figure $tu/D = 6.6939$ from the side view in Fig. 9 during the receding process because the fluid particles near the contact line do not have a full support and therefore their calculated normal vector will lose accuracy. The number of the particles left on the surface is 40–50 out of a total of 0.5 million particles (around 0.01%).

The spreading factor profile is shown in Fig. 11 and a good agreement is obtained where the relative error of the maximum spreading

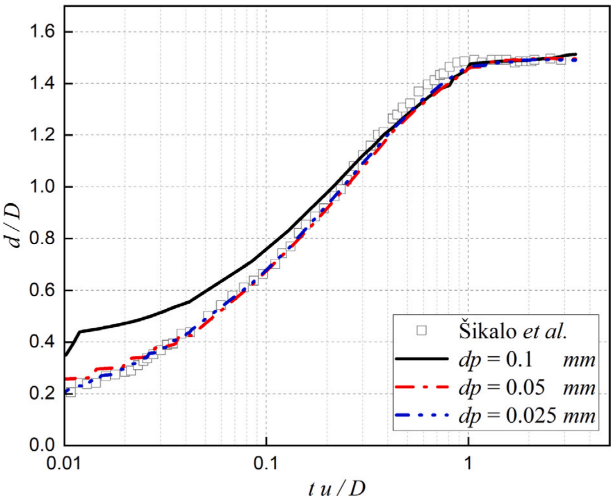

Fig. 7. Profile of the spreading factor $\beta_s = d/D$ for a glycerin droplet impacts on a solid wax surface.

Table 3
Parameters and values for the droplet migration case.

Parameters	Value
ρ	963 kg/m^3
σ	0.024 N/m
μ	0.04 Pa s
θ_{eq}	53°
k_T	1 W/(m K)
C_p	1670 J/(kg K)
$\frac{\partial\sigma}{\partial T}$	−0.047 mN/(m K)

factor is around 3%, when comparing with the experimental data of [38].

3.3. Droplet migration

A droplet migrating on a heated surface with the temperature gradient is investigated in this section. Following the experimental study from Tseng et al. [2] and the numerical study from Ting et al. [20], the physical properties used here are consistent with those reported in these two references, as shown in Table 3. In this test case, thermal radiation is neglected because conductive heat transfer dominates. The conduction-radiation interaction parameter $N = k_T/(4L_\circ\sigma_{SB}T_\circ^3)$, where σ_{SB} is the Stefan–Boltzmann constant, is $N \approx 120$, which means radiation contributes only 0.8% of the conductive heat flux scale. It should be noted that, as reported by several authors [45,46], the Marangoni effect is usually overestimated in numerical studies compared to experimental results due to surfactant contamination in the droplet in experiments which can significantly suppress the Marangoni effect. The effective Marangoni coefficient used numerically therefore should be reduced. In this study, we adopt the effective Marangoni coefficient $(\frac{\partial\sigma}{\partial T})_e$ of −0.0047 mN/(m K), which is 10% of the value reported in [45,46]. The surface tension coefficient is assumed to vary linearly with temperature, as expressed below,

$$\sigma = \sigma_0 + \frac{\partial\sigma}{\partial T}(T - T_0). \tag{47}$$

The temperature profile of the heated surface is obtained by extracting and fitting the data from [2,20] as shown in Fig. 12. At the beginning of the simulation, the droplet temperature is initialized to match the surface temperature profile, rather than the ambient temperature, in order to minimize the initial Marangoni force that would otherwise be induced by a large temperature gradient.

Three initial inter-particle distances are chosen as $dp = 0.05$ mm, 0.025 mm and 0.02 mm, respectively, corresponding to 8329, 64,813 and 125,889 fluid particles and 7352 s, 28,095 s, 57,905 s computational times. The smoothing length is $h = 2dp$. The initial droplet geometry is constructed as a spherical cap resting on the solid surface, with a prescribed equilibrium contact angle of $\theta_{eq} = 53°$. The total droplet volume is set to 1 μL.

Fig. 13 shows the Marangoni force and temperature profile at 0.01 s. It can be seen that the force is distributed according to the temperature gradient along the droplet surface and drives the droplet from the hot region towards the cold region. It is worth noting that, near the cold region (on the right side of the droplet), the Marangoni force points towards the solid wall. In simulations using DualSPHyiscs v5.2, this sometimes results in particle penetration. However, the newly implemented “no penetration” feature of English et al. [33] included in DualSPHysics v5.4, and described previously, can effectively prevent such a phenomenon.

Fig. 14-(a) shows the droplet displacement in comparison with the experimental results [2] and numerical results [20]. It can be observed that the SPH displacement result exhibits a convergent behaviour as dp reduces, obtaining good agreement with experiment and improving upon the numerical results of Long et al. [20] at the finest resolution. The deviation between the numerical and experimental results can be attributed to the uncertainty in determining the Marangoni coefficient, the presence of a partial-slip boundary condition in reality [4] (but no-slip in the model) and the absence of the secondary phase. The displacement profile at the early stage of $0 < t < 0.3$ s is shown in Fig. 14-(b). It can be seen that the droplet undergoes a relatively large displacement during the initial stage (approximately 0–0.025 s), which is attributed to the sudden strong Marangoni force at the beginning of the simulation and this results in a significant acceleration of the droplet. As the simulation progresses, this effect gradually diminishes.

To further justify the selection of the effective Marangoni coefficient, a sensitivity study is performed by varying the coefficient from 7.5% to 15% of the reference value. As shown in Fig. 15, the total displacement increases with the effective Marangoni coefficient, which further confirms that the thermo-capillary force is the primary driving force of the droplet migration. It can be observed that the case using coefficient 10% of the reference value shows the best agreement with the experimental results.

3.4. Droplet rapid spreading

In this section, a more challenging case involving the Marangoni effect is considered to show the limitation of the current model. Following Cheng et al. [47], the rapid spreading of a droplet on a heated surface is simulated. Two test conditions are considered: one without the Marangoni effect (Test 1) and another with a moderate Marangoni effect (Test 2). The corresponding parameters are shown in Table 4 based on the Ref. [47]. The inter-particle distance is $dp = 0.01$ mm, resulting in 423,171 fluid particles. The computational time are 6901 s and 7112 s for cases with and without the Marangoni effect, respectively.

Fig. 16 shows the comparison between the numerical spreading behaviour of the droplet, in the absence of the Marangoni effect, and the corresponding experimental results [47]. In the numerical results, after the initial rapid spreading, a relatively large satellite droplet is pinched off from the main droplet. Subsequently, the satellite droplet falls and coalesces with the main droplet. However, this phenomenon is inconsistent with the experimental observations, where the pinched-off satellite droplet rebounds from the main droplet due to the lubrication pressure. In addition, two other differences can be observed. First, the spreading diameter in the numerical results is larger than that in the experiments, which can be attributed to the assumption of a static contact angle in the model. Second, the time at which the satellite droplet is pinched off in the simulation occurs slightly later

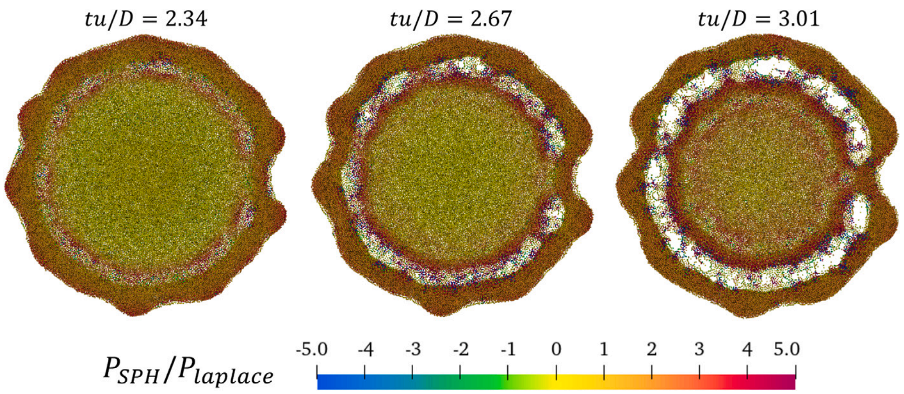

Fig. 8. The breakup of a water droplet impacts on a solid surface with the particle distance $dp = 0.05$ mm. $Re = 4010$.

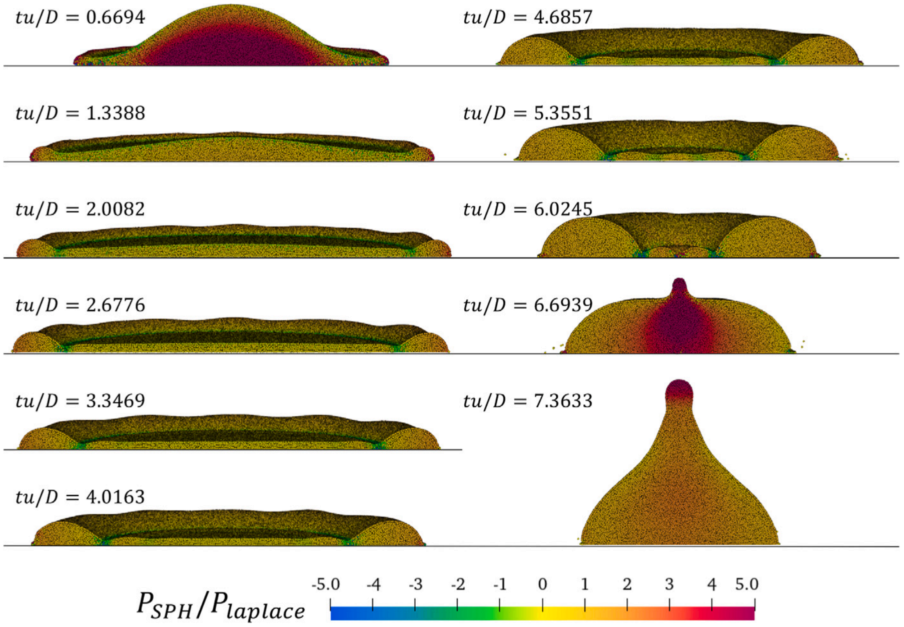

Fig. 9. The side view of a water droplet impacting on a solid surface with the pressure distribution. The particle distance is $dp = 0.025$ mm. $Re = 4010$.

Table 4
Parameters of two rapid spreading droplet test cases adopted from Cheng et al. [47].

Parameters	Test 1	Test 2
T_s	294 K	333 K
T_d	294 K	303 K
D_o	0.917 mm	0.815 mm
σ	0.0727 N/m	0.0712 N/m
θ_{eq}	20.1^o	25.1^o
ρ	998 kg/m^3	995.5 kg/m^3
μ	0.00098 Pa s	0.0008 Pa s
$\frac{\partial\sigma}{\partial T}$	-0.000171 N/(m K)	-0.000171 N/(m K)
Oh	0.00537	0.00471
Ma	0	0.072

(approximately 0.1–0.2 ms) than in the experiment as the effect of air on this phenomenon is absent.

Fig. 17 presents the comparison between the numerical spreading behaviour of the droplet with the Marangoni effect and the corresponding experimental results. It can be seen that the pinch-off phenomenon is suppressed in both the numerical and experimental results due to the Marangoni effect, with no pinch-off observed in the simulations. However, the experimental results show that a second-stage pinch-off occurs, in which the pinched-off satellite droplet is smaller than that observed in the case without Marangoni effect. Similar to the case without Marangoni effect, the assumption of a static contact angle and the absence of the second phase contribute to the difference in spreading diameter and pinch-off behaviour. In addition, the difficulty in accurately determining the numerical Marangoni coefficient also contributes to these deviations.

In summary, this test case demonstrates that the current single-phase model is capable of capturing the main features of rapid droplet spreading, such as pinch-off dynamics and the influence of the Marangoni effect, showing good agreement with experimental results in many aspects. However, the study also highlights the limitations of the model. When the secondary phase plays a significant role, certain experimental phenomena, such as the rebound of the satellite droplet from the main droplet due to lubrication pressure in the thin air layer, cannot be accurately reproduced.

4. Conclusion

In this work, a single-phase 3-D SPH scheme capable of modelling the droplet interaction with a heated solid surface has been developed.

Two benchmark cases are first considered to validate the proposed scheme, the natural convection in a cavity and droplet impact on a

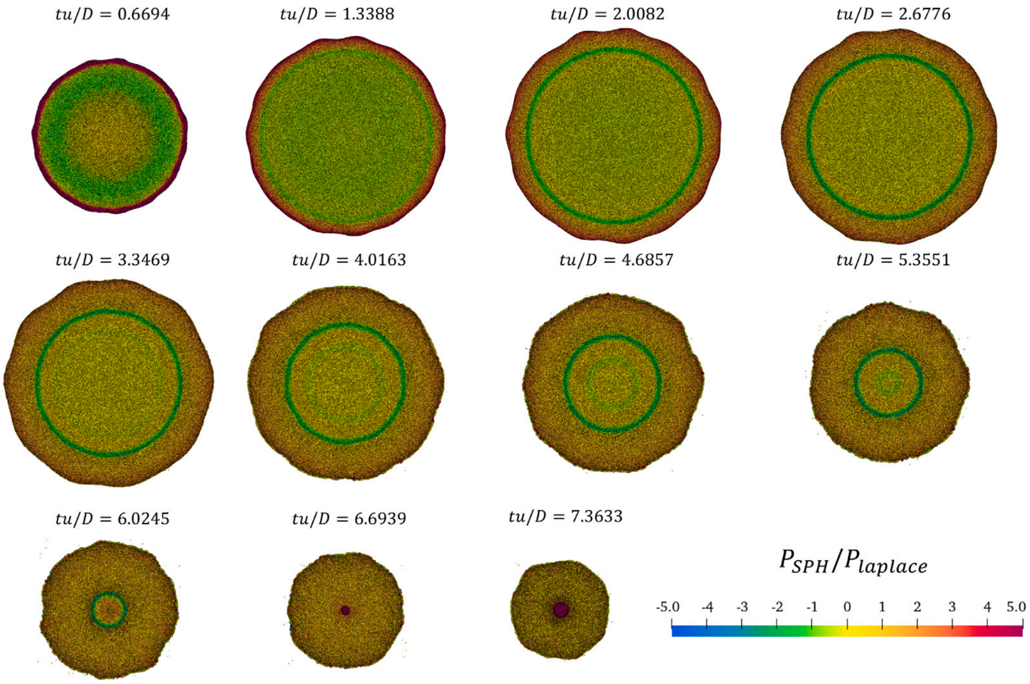

Fig. 10. The top view of water droplet impacting on a solid surface with the pressure distribution. The particle distance is $dp = 0.025$ mm. $Re = 4010$.

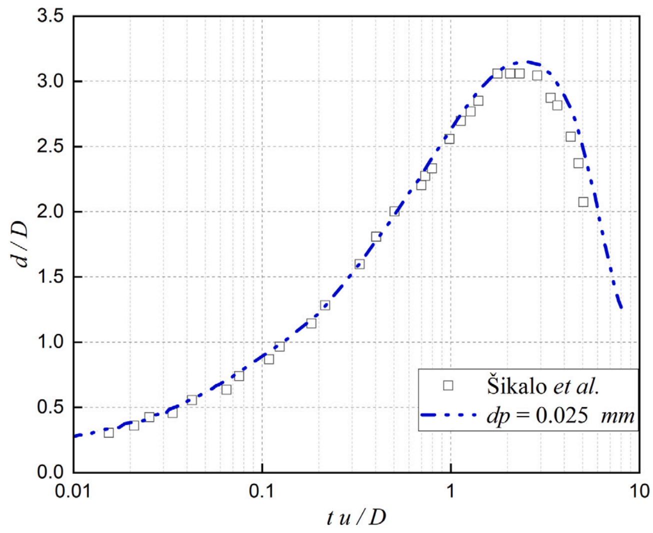

Fig. 11. Profile of the spreading factor $\beta_s = d/D$ for a water droplet impact on a solid wax surface comparing with the experimental data of [38] for $Re = 4010$.

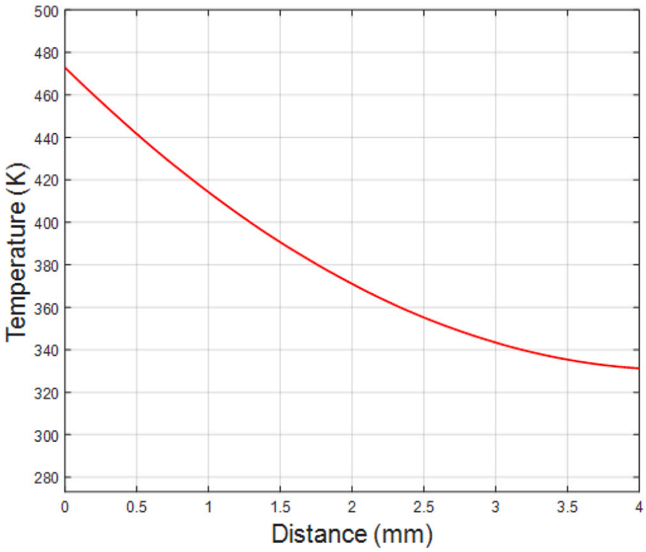

Fig. 12. Surface temperature profile extracted from Tseng et al. [2] & Long et al. [20].

solid surface. The numerical results show good agreement with the reference data, where the relative error is within 3%–5%. Subsequently, the behaviour of the droplet migration phenomenon in 3-D is investigated. Under the influence of a solid surface temperature gradient, the droplet migrates from the hot region towards the cold region. The numerical prediction of the total displacement demonstrates convergent behaviour and agrees well with experimental results. However, minor deviations are observed, which are primarily attributed to the sudden Marangoni force at the beginning of the simulation, uncertainties in determining the numerical Marangoni coefficient and the presence of partial-slip boundary conditions.

The final case, concerning the rapid droplet spreading with and without the Marangoni effect, is a very challenge case which further shows the limitation of the proposed numerical model. The current model is capable of capturing the main features of the case, such as pinch-off behaviour and its suppression due to the Marangoni effect. However, when the secondary phase plays an important role, such as in the rebound of the satellite droplet, this single-phase model is unable to capture all the experimental physics. These differences can be attributed to the single-phase assumption, as well as the use of a static contact angle and uncertainties in the determination of the Marangoni coefficient.

Overall, the present single-phase model has proven to be robust and efficient across a variety of benchmark problems, demonstrating good agreement with reference results. Its computational efficiency makes it particularly appropriate for large 3-D simulations. However, to further improve the accuracy and physical fidelity of the model, future work should focus on extending the model to incorporate multiphase effects, a dynamic contact angle and more realistic wall boundary conditions.

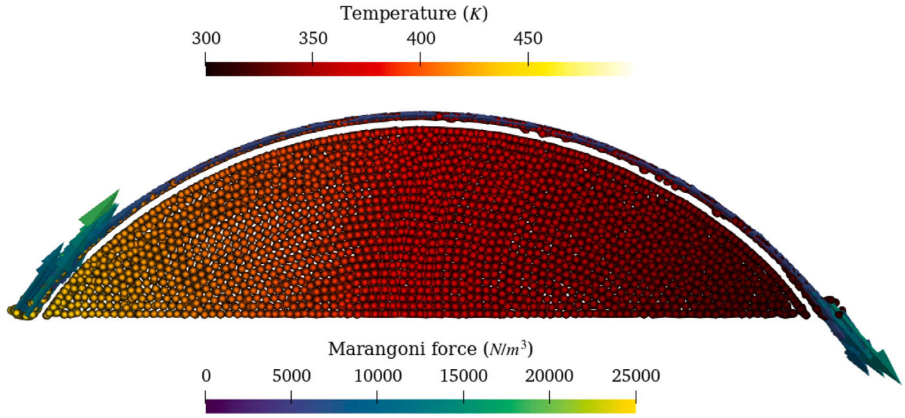

Fig. 13. Marangoni force and temperature profile on a droplet cross-section on a heated surface at $t = 0.01$ s with $dp = 0.02$ mm.

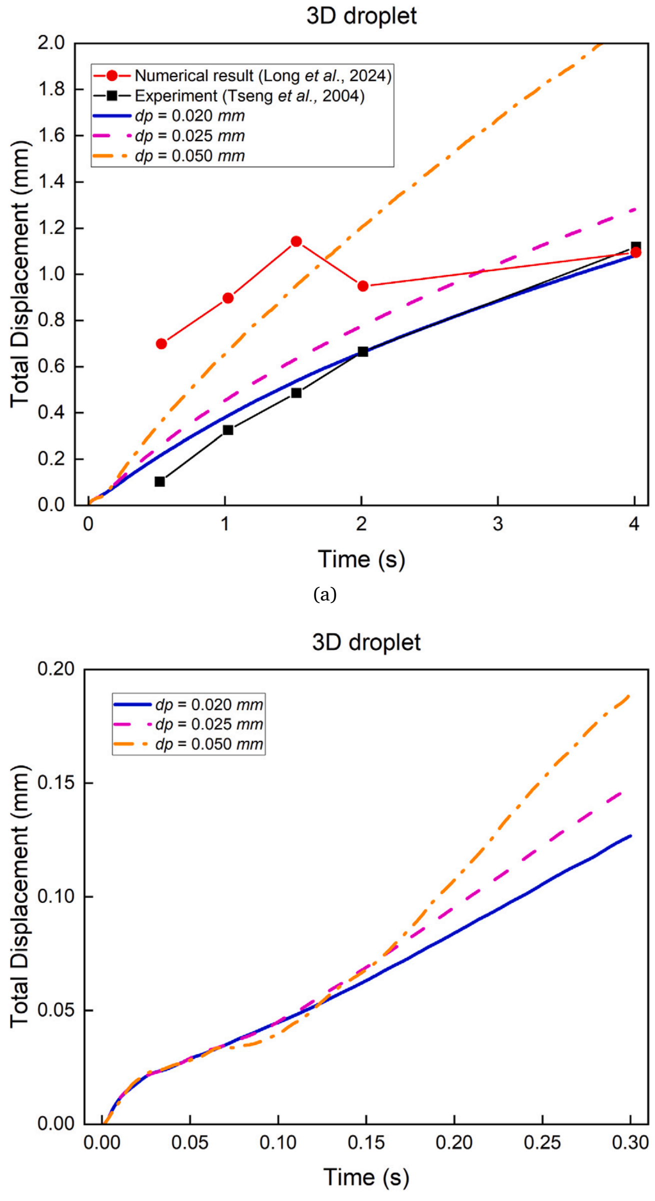

(a)

(b)

Fig. 14. Displacement profile for droplet migration case with three resolutions over two distinct time intervals (a) from 0–4 s (b) from 0–0.3 s.

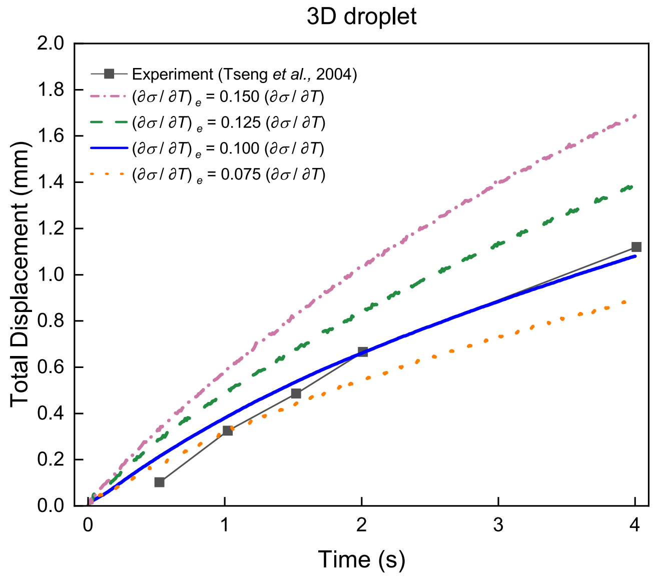

Fig. 15. Sensitivity study of the effective Marangoni coefficient on the total displacement of a 3-D droplet with $dp = 0.02$ mm.

CRediT authorship contribution statement

Chunze Cen: Writing – review & editing, Writing – original draft, Validation, Software, Methodology, Investigation, Conceptualization. **Aaron English:** Writing – review & editing, Methodology. **Georgios Fourtakas:** Writing – review & editing, Supervision, Methodology, Conceptualization. **Steven Lind:** Writing – review & editing, Supervision, Methodology, Conceptualization. **Benedict D. Rogers:** Writing – review & editing, Supervision, Methodology, Conceptualization.

Declaration of competing interest

The authors declare that they have no known competing financial interests or personal relationships that could have appeared to influence the work reported in this paper.

Acknowledgements

Dr Cen would like to acknowledge the financial support provided by the China Scholarship Council and the University of Manchester, United Kingdom joint scholarship fund. Dr English acknowledges financial support from PNRR MUR project ECS_00000033_ECOSISTER funded by the European Union – NextGenerationEU.

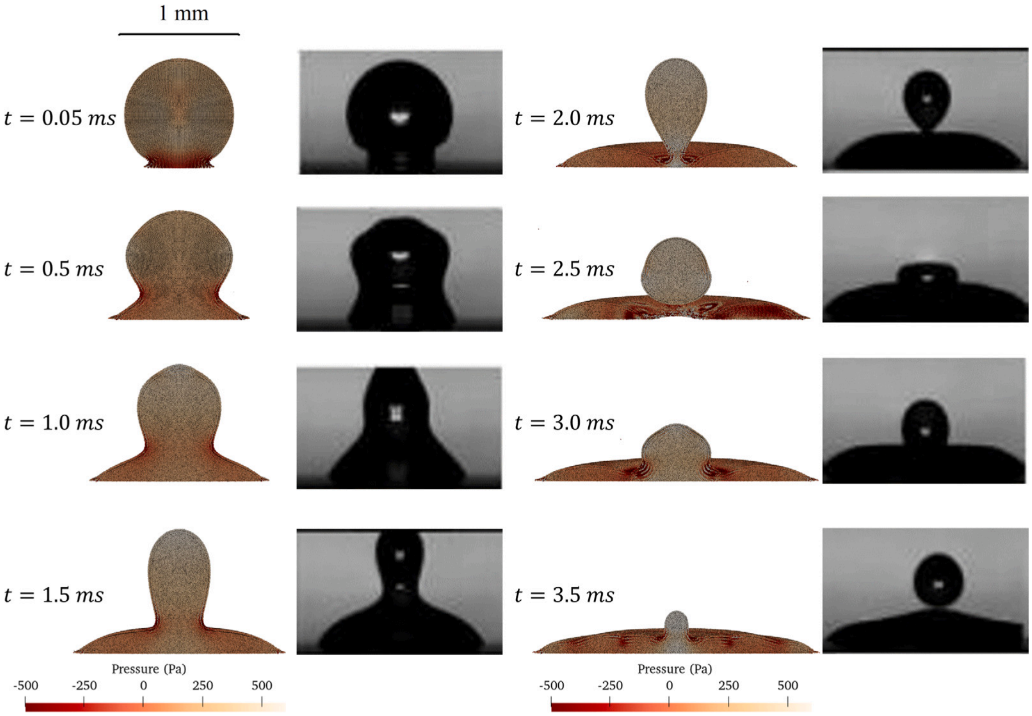

Fig. 16. Comparison of droplet profiles on a surface without the Marangoni effect between SPH results and experimental results. *Source:* The experimental results are adapted from [47].

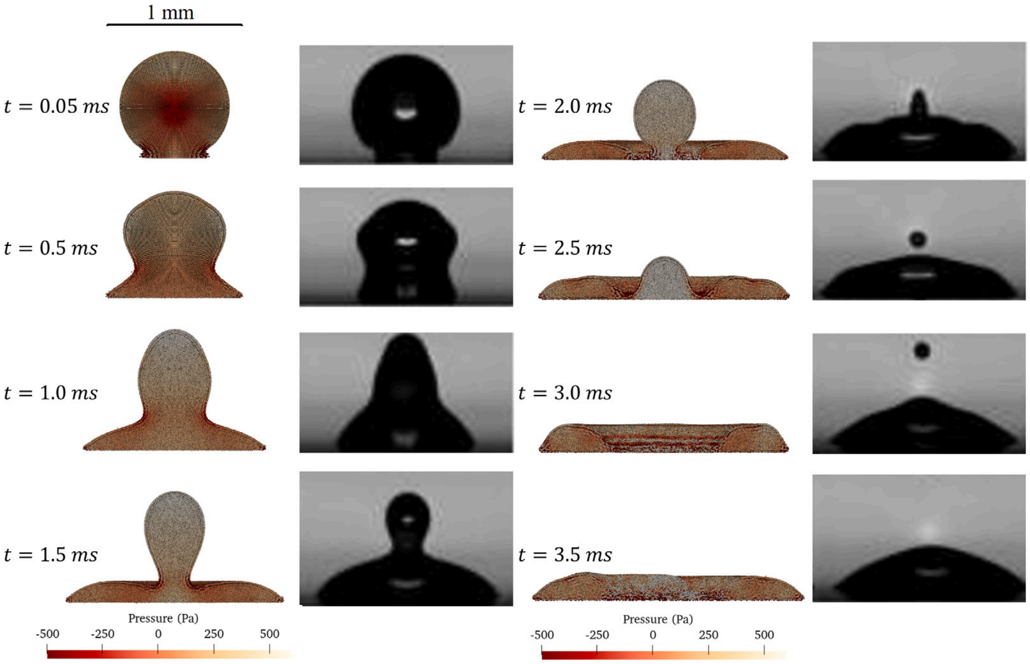

Fig. 17. Comparison of a droplet profiles on surface with the Marangoni effect between SPH results and experimental results. *Source:* The experimental results are adapted from [47].

References

[1] A. Karbalaei, R. Kumar, H.J. Cho, Thermocapillarity in microfluidics—A review, Micromachines 7 (1) (2016) 13.

[2] Y.-T. Tseng, F.-G. Tseng, Y.-F. Chen, C.-C. Chieng, Fundamental studies on micro-droplet movement by marangoni and capillary effects, Sensors Actuators A: Phys. 114 (2–3) (2004) 292–301.

[3] M. Sussman, P. Smereka, S. Osher, A level set approach for computing solutions to incompressible two-phase flow, J. Comput. Phys. 114 (1) (1994) 146–159.

[4] Y. Sui, Moving towards the cold region or the hot region? Thermocapillary migration of a droplet attached on a horizontal substrate, Phys. Fluids 26 (9) (2014).

[5] A. Fath, D. Bothe, Direct numerical simulations of thermocapillary migration of a droplet attached to a solid wall, Int. J. Multiph. Flow 77 (2015) 209–221.

[6] C.W. Hirt, B.D. Nichols, Volume of fluid (VOF) method for the dynamics of free boundaries, J. Comput. Phys. 39 (1) (1981) 201–225.

[7] T.-L. Le, J.-C. Chen, B.-C. Shen, F.-S. Hwu, H.-B. Nguyen, Numerical investigation of the thermocapillary actuation behavior of a droplet in a microchannel, Int. J. Heat Mass Transfer 83 (2015) 721–730.

[8] X. Fu, J. Zeng, H. Yang, G. Zhai, C. Lai, Numerical study of droplet thermocapillary migration on rectangular wettability-confined tracks using a lattice Boltzmann model, Phys. Fluids 37 (8) (2025).

[9] J.U. Brackbill, D.B. Kothe, C. Zemach, A continuum method for modeling surface tension, J. Comput. Phys. 100 (2) (1992) 335–354.

[10] J.P. Morris, Simulating surface tension with smoothed particle hydrodynamics, Internat. J. Numer. Methods Fluids 33 (3) (2000) 333–353.

[11] X.Y. Hu, N.A. Adams, A multi-phase SPH method for macroscopic and mesoscopic flows, J. Comput. Phys. 213 (2) (2006) 844–861.

[12] S. Adami, X. Hu, N.A. Adams, A new surface-tension formulation for multi-phase SPH using a reproducing divergence approximation, J. Comput. Phys. 229 (13) (2010) 5011–5021.

[13] C. Zöller, N. Adams, S. Adami, A partitioned continuous surface stress model for multiphase smoothed particle hydrodynamics, J. Comput. Phys. 472 (2023) 111716.

[14] W. Sun, L. Zhang, K. Liew, Fast detection of free surface and surface tension modelling via single-phase SPH, Appl. Math. Model. 100 (2021) 33–54.

[15] M. Ordoubadi, M. Yaghoubi, F. Yeganehdoust, Surface tension simulation of free surface flows using smoothed particle hydrodynamics, Sci. Iran. 24 (4) (2017) 2019–2033.

[16] N.N. Ehigiamusoe, S. Maxutov, Y.C. Lee, Modeling surface tension of a two-dimensional droplet using smoothed particle hydrodynamics, Internat. J. Numer. Methods Fluids 88 (7) (2018) 334–346.

[17] M. Tong, D.J. Browne, An incompressible multi-phase smoothed particle hydrodynamics (SPH) method for modelling thermocapillary flow, Int. J. Heat Mass Transfer 73 (2014) 284–292.

[18] M. Hopp-Hirschler, M.S. Shadloo, U. Nieken, A smoothed particle hydrodynamics approach for thermo-capillary flows, Comput. & Fluids 176 (2018) 1–19.

[19] C. Meier, S.L. Fuchs, A.J. Hart, W.A. Wall, A novel smoothed particle hydrodynamics formulation for thermo-capillary phase change problems with focus on metal additive manufacturing melt pool modeling, Comput. Methods Appl. Mech. Engrg. 381 (2021) 113812.

[20] T. Long, Y. Qin, J. Wan, Numerical simulations of thermal capillary migration of a droplet on a temperature gradient wall with smoothed particle hydrodynamics method, Phys. Fluids 36 (4) (2024).

[21] C. Bierwisch, Consistent thermo-capillarity and thermal boundary conditions for single-phase smoothed particle hydrodynamics, Materials 14 (16) (2021) 4530.

[22] P.W. Cleary, J.J. Monaghan, Conduction modelling using smoothed particle hydrodynamics, J. Comput. Phys. 148 (1) (1999) 227–264.

[23] P. Sun, C. Pilloton, M. Antuono, A. Colagrossi, Inclusion of an acoustic damper term in weakly-compressible SPH models, J. Comput. Phys. 483 (2023) 112056.

[24] J.M. Domínguez, G. Fourtakas, C. Altomare, R.B. Canelas, A. Tafuni, O. García-Feal, I. Martínez-Estévez, A. Mokos, R. Vacondio, A.J. Crespo, et al., DualSPHysics: from fluid dynamics to multiphysics problems, Comput. Part. Mech. (2021) 1–29.

[25] A. Vergnaud, G. Oger, D. Le Touzé, M. DeLeffe, L. Chiron, C-CSF: Accurate, robust and efficient surface tension and contact angle models for single-phase flows using SPH, Comput. Methods Appl. Mech. Engrg. 389 (2022) 114292.

[26] C. Cen, G. Fourtakas, S. Lind, B.D. Rogers, A single-phase GPU-accelerated surface tension model using SPH, Comput. Phys. Comm. 295 (2024) 109012.

[27] E.Y. Lo, S. Shao, Simulation of near-shore solitary wave mechanics by an incompressible SPH method, Appl. Ocean Res. 24 (5) (2002) 275–286.

[28] T. Breinlinger, P. Polfer, A. Hashibon, T. Kraft, Surface tension and wetting effects with smoothed particle hydrodynamics, J. Comput. Phys. 243 (2013) 14–27.

[29] S.J. Lind, R. Xu, P.K. Stansby, B.D. Rogers, Incompressible smoothed particle hydrodynamics for free-surface flows: A generalised diffusion-based algorithm for stability and validations for impulsive flows and propagating waves, J. Comput. Phys. 231 (4) (2012) 1499–1523.

[30] A. Khayyer, H. Gotoh, Y. Shimizu, Comparative study on accuracy and conservation properties of two particle regularization schemes and proposal of an optimized particle shifting scheme in ISPH context, J. Comput. Phys. 332 (2017) 236–256.

[31] A. English, J. Domínguez, R. Vacondio, A. Crespo, P. Stansby, S. Lind, L. Chiapponi, M. Gómez-Gesteira, Modified dynamic boundary conditions (mDBC) for general-purpose smoothed particle hydrodynamics (SPH): application to tank sloshing, dam break and fish pass problems, Comput. Part. Mech. (2021) 1–15.

[32] M. Liu, G.-R. Liu, Restoring particle consistency in smoothed particle hydrodynamics, Appl. Numer. Math. 56 (1) (2006) 19–36.

[33] A. English, R. Vacondio, S. Dazzi, J.M. Dominguez, Smoothed particle hydrodynamics modelling of river flows past bridges, Comput. & Fluids (2025) 106870.

[34] A.R. English, Design of Low Residue Packs by Smoothed Particle Hydrodynamics, The University of Manchester (United Kingdom), 2020.

[35] G.R. Reece, Modelling and Investigation of Multi-Phase Mixing for Vitrification Applications Using Smoothed Partile Hydrodynamics (SPH) (Ph.D. thesis), Ph.D. thesis, University of Manchester, 2022.

[36] B. Leimkuhler, C. Matthews, Molecular dynamics, Interdiscip. Appl. Math. 39 (2015) 443.

[37] D. Wan, B. Patnaik, G. Wei, A new benchmark quality solution for the buoyancy-driven cavity by discrete singular convolution, Numer. Heat Transf.: Part B: Fundam. 40 (3) (2001) 199–228.

[38] v. Šikalo, H.-D. Wilhelm, I. Roisman, S. Jakirlić, C. Tropea, Dynamic contact angle of spreading droplets: Experiments and simulations, Phys. Fluids 17 (6) (2005).

[39] P. Sun, A. Colagrossi, S. Marrone, A. Zhang, The δplus-SPH model: Simple procedures for a further improvement of the SPH scheme, Comput. Methods Appl. Mech. Engrg. 315 (2017) 25–49.

[40] S.T. Thoroddsen, K. Takehara, T. Etoh, Bubble entrapment through topological change, Phys. Fluids 22 (5) (2010).

[41] A.I. Fedorchenko, A.-B. Wang, Y.-H. Wang, Effect of capillary and viscous forces on spreading of a liquid drop impinging on a solid surface, Phys. Fluids 17 (9) (2005).

[42] J. Eggers, M.A. Fontelos, C. Josserand, S. Zaleski, Drop dynamics after impact on a solid wall: theory and simulations, Phys. Fluids 22 (6) (2010).

[43] G. Lagubeau, M.A. Fontelos, C. Josserand, A. Maurel, V. Pagneux, P. Petitjeans, Spreading dynamics of drop impacts, J. Fluid Mech. 713 (2012) 50–60.

[44] C. Josserand, S.T. Thoroddsen, Drop impact on a solid surface, Annu. Rev. Fluid Mech. 48 (1) (2016) 365–391.

[45] H. Hu, R.G. Larson, Analysis of the effects of marangoni stresses on the microflow in an evaporating sessile droplet, Langmuir 21 (9) (2005) 3972–3980.

[46] H. Hu, R.G. Larson, Analysis of the microfluid flow in an evaporating sessile droplet, Langmuir 21 (9) (2005) 3963–3971.

[47] Y. Cheng, E. Li, J. Wang, P. Yu, Y. Sui, Rapid droplet spreading on a hot substrate, Phys. Fluids 33 (9) (2021).